International Journal of Hydrogen Energy 202 (2026) 153033

Contents lists available at ScienceDirect

International Journal of Hydrogen Energy

journal homepage: www.elsevier.com/locate/he

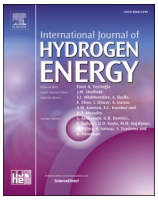

First-principles study on structural, electronic, mechanical, optical, vibrational, thermal, and hydrogen storage properties of Li_2SnH_4 and Na_2SnH_4 compounds

Cengiz Soykan [a], Cihan Kürkçü [b,*]

[a] Department of Medical Services and Techniques, Kırşehir Ahi Evran University, Kırşehir, Türkiye
[b] Department of Electronics and Automation, Kırşehir Ahi Evran University, Kırşehir, Türkiye

ARTICLE INFO

Keywords:
Hydrogen storage
Electronic properties
Elastic properties
Optical properties
Vibrational properties
Thermal properties

ABSTRACT

This study presents a comprehensive first-principles investigation of the structural, electronic, mechanical, vibrational, thermal, and hydrogen storage properties of X_2SnH_4 (X = Li and Na) hydrides in the tetragonal $P4_2/mnm$ phase. Thermodynamic stability is confirmed by negative formation energies (−0.002 eV/atom for Li_2SnH_4 and –0.049 eV/atom for Na_2SnH_4), while phonon spectra without imaginary modes demonstrate dynamic stability. Electronic analyses reveal semiconducting behavior with band gaps of 0.678 eV (Li_2SnH_4) and 1.251 eV (Na_2SnH_4). Mechanical stability is verified by Born criteria, and Li_2SnH_4 exhibits higher stiffness (B = 59.0 GPa, G = 29.8 GPa) compared to Na_2SnH_4 (B = 38.3 GPa, G = 20.1 GPa). Vibrational and thermal results indicate stronger H–Sn bonding and higher lattice rigidity in Li_2SnH_4, supported by its larger Debye temperature (~2300 K) relative to Na_2SnH_4 (~1600 K). Hydrogen storage analysis yields gravimetric capacities of 5.95 wt% for Li_2SnH_4 and 4.82 wt% for Na_2SnH_4, highlighting their potential as lightweight hydrogen storage materials. Overall, the combined electronic, mechanical, thermal, and storage properties identify X_2SnH_4 compounds, particularly Li_2SnH_4, as promising candidates for next-generation solid-state hydrogen storage applications.

1. Introduction

The increasing global demand for energy and the environmental concerns caused by fossil fuels have intensified the need for low-carbon and sustainable energy solutions. Hydrogen has emerged as a promising energy carrier due to its high gravimetric energy density, its potential to be produced from renewable resources, and its environmentally friendly utilization where only water is released as the by-product in fuel cells [1–3]. However, the safe, economical, and practical storage of hydrogen remains one of the major obstacles to the widespread adoption of the hydrogen economy [4]. For this reason, research on solid-state hydrogen storage materials has gained significant attention. Among solid-state hydrogen storage materials, metal hydrides, complex hydrides, borohydrides, and alloy-based compounds have been widely studied both theoretically and experimentally [5–7]. Although these materials offer high gravimetric hydrogen capacities, their practical applications are often limited by high desorption temperatures, sluggish kinetics, and poor reversibility. $NaAlH_4$, for instance, provides about 5.6 wt% hydrogen capacity but suffers from kinetic barriers that hinder its reversibility [5]. $LiBH_4$ possesses a very high hydrogen capacity (18.5 wt %), yet its high desorption temperature and poor reversibility restrict its practical use [5]. MgH_2 is inexpensive and has a relatively high hydrogen capacity, but its large desorption enthalpy necessitates additional modifications [8]. These challenges highlight the urgent need for novel materials that can simultaneously provide sufficient capacity, moderate thermodynamic stability, and favorable desorption kinetics.

Hydrides and complex hydrides containing tin (Sn) have been much less explored in the literature, although they present interesting opportunities for hydrogen storage applications. Previous high-pressure studies on hydrogen-rich Sn–H compounds (e.g., SnH_4) have demonstrated the significant influence of Sn–H bonding on electronic properties and phase stability [9]. However, systematic first-principles investigations of Li–Sn–H and Na–Sn–H compounds under ambient conditions are still scarce. More recent studies on Sn-based perovskite-like hydrides suggest that Sn incorporation can modulate phonon behavior, bonding strength, and hydrogen storage performance, pointing toward their potential as new hydrogen storage candidates [10]. Furthermore, the incorporation of light alkali metals such as Li and

* Corresponding author.
E-mail address: ckurkcu@ahievran.edu.tr (C. Kürkçü).

https://doi.org/10.1016/j.ijhydene.2025.153033
Received 1 October 2025; Received in revised form 5 December 2025; Accepted 12 December 2025
Available online 16 December 2025

Na into Sn–H frameworks is expected to enhance gravimetric capacity and tune bonding characteristics, thereby offering complementary advantages in terms of storage density and desorption kinetics [11].

Recent first-principles investigations have significantly advanced the understanding of structural and hydrogen-storage properties of these materials. For example, Almahmoud et al. [12] systematically examined the perovskite hydrides Y_2CoH_6 (Y═Ca, Ba, Mg, Sr) and demonstrated their mechanical, dynamical, and thermodynamic stability along with gravimetric hydrogen capacities ranging from 1.77 to 5.32 wt%. Their metallic electronic character and robust lattice stability highlight their potential for efficient hydrogen absorption pathways and high durability under operational conditions. Al-Zoubi et al. [13] conducted a comprehensive DFT analysis of $NaXH_3$ and KXH_3 (X = Tc, Ru, Rh) and confirmed that these hydrides also exhibit stable cubic structures, negative formation energies, and favorable hydrogen storage capacities. Notably, $KTcH_3$ was reported to possess a low desorption temperature of 365 K, while all compounds showed metallic conductivity and strong optical response, indicating multifunctional applicability beyond hydrogen storage. Obeidat et al. [14] investigated $K_2BAl_{1-x}Ga_xH_6$ (B═Li, Na) and reported tunable structural transitions, negative formation energies, and gravimetric capacities reaching 5.12 wt%, with desorption temperatures spanning 191–413 K depending on Ga substitution. These findings highlight that B/B′-site alloying is an effective strategy to tailor hydrogen bonding strength and desorption thermodynamics in lightweight hydrides. The study on $K_2NaA_{1-x}B_xH_6$ (A, B═Al, Ga, Sc) demonstrated that Sc- and Ga-substitution provides broad control over electronic band gaps (0.93–2.84 eV), mechanical stiffness, and hydrogen storage capacities (3.42–4.51 wt%). Notably, Al-rich compounds exhibited the strongest thermodynamic stability, whereas Sc substitution lowered desorption temperatures, indicating improved hydrogen release kinetics [15]. Cs_2XAlH_6 (X = K, Na, Rb) [16] compounds possess a stable cubic structure, exhibit negative formation energies, and can store approximately 1.6–1.9 wt% hydrogen. Similarly, KX_3H_8 (X = Sc, V, Cr) hydrides [17] have been shown to offer hydrogen storage capacities in the range of 3.9–4.43 wt%, display metallic electronic behavior, and exhibit dynamic stability according to phonon calculations. X_2FeH_5 (X = Ca, Mg, Ba) hydrides [18] have shown that these compounds crystallize in a stable tetragonal *P4/nmm* structure, possess negative formation enthalpies, and offer hydrogen storage capacities between 1.50 and 4.60 wt% with desorption temperatures of 240–460 K, alongside metallic or half-metallic electronic behavior. X_2CaAlH_6 (Y═K, Rb, Cs) hydrides [19] indicate that these materials are thermodynamically and dynamically stable in the cubic Fm-3m phase, exhibit mixed ionic–covalent bonding and metallic conductivity, and provide gravimetric hydrogen capacities of 1.78–5.39 wt% with desorption temperatures around 402.7–620 K.

A wide range of perovskite- and complex-type hydrides has been investigated as potential lightweight and thermodynamically stable materials for solid-state hydrogen storage. Among Na-based systems, $NaYH_3$ and $NaWH_3$ [20] have attracted attention due to their structural stability and transition-metal–dependent electronic behavior, although detailed hydrogen storage data for these hydrides remain limited. In contrast, heavier alkaline-earth hydrides such as $BaXH_3$ (X = Tc, Ta, Mo) [21] exhibit metallic electronic characteristics but provide only 0.93–1.26 wt% gravimetric hydrogen capacities, which strongly limits their practical usability in lightweight storage applications. More promising performance has been reported for $MgXH_3$ (X = Al, Sc, Zr) perovskites [22], which deliver gravimetric capacities of 5.274 wt%, 4.015 wt%, and 2.487 wt%, respectively, positioning them among the most competitive ABH_3-type hydrides available to date. Meanwhile, K-based perovskite hydrides such as $KMnH_3$ and $KFeH_3$ [23] exhibit moderate hydrogen storage capacities of 3.021 wt% and 2.994 wt%, respectively, along with thermodynamic and mechanical stabilities suitable for practical applications. Another relevant family includes the complex cobalt hydrides X_2CoH_5 (X = Ca, Sr) [24], whose gravimetric capacities of 3.38 wt% and 2.06 wt% further demonstrate the performance limitations of many existing hydrides when compared to the targets required for efficient hydrogen storage. Collectively, these findings illustrate that although numerous hydrides offer structural and thermodynamic stability, their hydrogen storage capacities remain insufficient. In this context, the markedly higher gravimetric densities obtained in the present work for Li_2SnH_4 (5.95 wt%) and Na_2SnH_4 (4.82 wt%) clearly highlight the superior potential of Sn-based hydrides relative to these previously investigated systems.

This work aims to comprehensively investigate the hydrogen storage potential of X_2SnH_4 using density functional theory (DFT) based first-principles calculations. In this context, the structural, electronic, mechanical, vibrational, optical, and thermal properties of both compounds have been systematically examined, and their hydrogen storage performance has been evaluated in terms of gravimetric capacity, stability, and kinetic factors. This study thus provides the first detailed theoretical assessment of X_2SnH_4, supplying novel insights into their suitability as hydrogen storage materials and contributing to the development of new candidates within the family of Sn-based hydrides.

2. Methods

The evaluation of total energies was conducted via the CASTEP computational package, which utilizes Density Functional Theory (DFT) within the framework of plane-wave basis sets and pseudopotentials [25–28]. For describing the exchange-correlation interactions, the Generalized Gradient Approximation (GGA) formulated by Perdew, Burke, and Ernzerhof (PBE) was adopted [29]. During the structural optimization steps, plane-wave cut-off energies were chosen as 720 eV and 770 eV for Li_2SnH_4 and Na_2SnH_4, respectively, to ensure reliable computation of both energy and stress parameters. These values were selected based on systematic convergence tests with respect to plane-wave cut-off energy and k-point sampling. In computational studies of crystalline systems, analyzing the periodic characteristics associated with the Bloch wave vector across the Brillouin zone (BZ) or within selected portions of it is typically sufficient. To enhance computational performance, particularly when calculations at each BZ point are demanding, these evaluations are conducted over a finite and strategically chosen to set of k-points within the BZ [30]. In the present work, sampling of the reciprocal space was carried out using Monkhorst-Pack k-point meshes of $8 \times 8 \times 5$ for Li_2SnH_4 and $8 \times 8 \times 6$ for Na_2SnH_4, with these grids tailored to match the respective supercell geometries. Ultrasoft pseudopotentials were employed to represent the interactions between valence electrons and ionic cores. The considered valence electron configurations were as follows: Li ($2s^1$), Sn ($5s^2\ 5p^6$), Na ($2s^2\ 2p^6\ 3s^1$), and H ($1s^1$). Structural optimization processes were carried out using the Broyden–Fletcher–Goldfarb–Shanno (BFGS) algorithm, ensuring ultra-fine calculation accuracy. The convergence thresholds were established as 5.0×10^{-7} eV/atom for the electronic self-consistent field, 0.01 eV/Å for the maximum force acting on atoms, 0.01 GPa for the upper limit of internal stress, and 5.0×10^{-4} Å for the maximum atomic displacement [31]. To account for long-range van der Waals interactions, the Tkatchenko–Scheffler (TS) dispersion correction within the DFT-D framework was applied. This method refines standard DFT calculations by incorporating environment-dependent dispersion coefficients, thereby improving the accuracy of structural and energetic predictions, particularly in weakly bonded systems [32]. The optical and vibrational (phonon) characteristics of the structures were analyzed through single-point energy computations employing norm-conserving pseudopotentials. Additionally, elastic constants (C_{ij}) and associated mechanical parameters were evaluated to assess the mechanical stability and response of the investigated phases. To gain insight into the electronic behavior of X_2SnH_4, electronic structure analyses were carried out by computing the total density of states (*DOS*) as well as the partial density of states (*pDOS*). Moreover, calculations of Heat Capacity and Debye Temperature were conducted to investigate variations in the thermal stability of the materials. In the final stage of the study, the

hydrogen storage potential of the X_2SnH_4 compounds was assessed based on their calculated physical properties. Detailed structural information such as atomic coordinates, space group symmetries, and lattice constants was obtained using the VESTA visualization program [33].

3. Results and discussion

3.1. Structural properties

Fig. 1 shows the crystal structure of the tetragonal type X_2SnH_4 compounds with space group $P4_2/mnm$. The unit cell contains 14 atoms. For the compound Li_2SnH_4, the Li, Sn, and H atoms are represented by the following Wyckoff positions: Li at 4d (0.5, 0, 0.25), Sn at 2a (0, 0, 0), H1 at 4f (0.2853, 0.2853, 0), and H2 at 4e (0, 0, 0.28878). For the compound Na_2SnH_4, the Na, Sn, and H atoms are represented by the following Wyckoff positions: Na at 4d (0.5, 0, 0.25), Sn at 2a (0, 0, 0), H1 at 4f (0.24392, 0.24392, 0), and H2 at 4e (0, 0, 0.25011). Table 1 presents the fractional atomic coordinates of Li_2SnH_4 and Na_2SnH_4 in the $P4_2/mnm$ structure, each containing 8H, 4 Li/Na, and 2 Sn atoms per unit cell.

Table 2 shows the lattice parameter values that were found for the X_2SnH_4 compounds. This study calculated the physical properties of these compounds for the first time, so there was no data for comparison in the table.

We also calculated the formation energy value to see if the $P4_2/mnm$ phase of the X_2SnH_4 compounds is stable in terms of thermodynamics. As a result of the calculations, the formation energy for this structure was obtained as −0.002 and −0.049 using eq. (1) for Li_2SnH_4 and Na_2SnH_4 compounds, respectively. These values are relatively small and may lie within the intrinsic uncertainty (~10–50 meV/atom) associated with standard DFT-GGA predictions. Therefore, the formation energy alone is not used as a decisive indicator of stability. Nevertheless, the slightly negative values do suggest that the hydrides are not energetically disfavored relative to their elemental constituents. More importantly, their mechanical (elastic constants satisfying the Born criteria), dynamical (absence of imaginary phonon modes), and thermal indicators consistently confirm the stability of the $P4_2/mnm$ phase. Considering these factors, experimental synthesis of these compounds appears plausible, especially under hydrogen-rich or mild-pressure synthesis environments.

$$E_f = \frac{1}{(n_X + n_{Sn} + n_{H_2})}\left[E_{tot}(X_2SnH_4) - n_X E_{tot}(X) - n_{Sn}E_{tot}(Sn) - n_{H_2}E_{tot}(H_2)\right] \quad (1)$$

Table 1
Fractional atomic coordinates for Li_2SnH_4 and Na_2SnH_4 in the $P4_2/mnm$ structure.

Compound	Atom	x	y	z
Li_2SnH_4	H1	0.285300	0.285300	0.000000
	H2	0.714700	0.714700	0.000000
	H3	0.214700	0.785300	0.500000
	H4	0.785300	0.214700	0.500000
	H5	0.000000	0.000000	0.288780
	H6	0.000000	0.000000	0.711220
	H7	0.500000	0.500000	0.788780
	H8	0.500000	0.500000	0.211220
	Li1	0.500000	0.000000	0.250000
	Li2	0.500000	0.000000	0.750000
	Li3	0.000000	0.500000	0.250000
	Li4	0.000000	0.500000	0.750000
	Sn1	0.000000	0.000000	0.000000
	Sn2	0.500000	0.500000	0.500000
Na_2SnH_4	H1	0.243920	0.243920	0.000000
	H2	0.756080	0.756080	0.000000
	H3	0.256080	0.743920	0.500000
	H4	0.743920	0.256080	0.500000
	H5	0.000000	0.000000	0.250110
	H6	0.000000	0.000000	0.749890
	H7	0.500000	0.500000	0.750110
	H8	0.500000	0.500000	0.249890
	Na1	0.500000	0.000000	0.250000
	Na2	0.500000	0.000000	0.750000
	Na3	0.000000	0.500000	0.250000
	Na4	0.000000	0.500000	0.750000
	Sn1	0.000000	0.000000	0.000000
	Sn2	0.500000	0.500000	0.500000

E_{H2} shows the total energy of the hydrogen molecule, while E_X and E_{Sn} show the total energy of the X and S elements in their ground state, respectively. The n_X, n_{Sn}, and n_{H_2} stand for the number of X, Sn, and H atoms in the unit cell. $E_{tot}(X_2SnH_4)$ shows how much energy X_2SnH_4 has in total. The value of the formation energy for X_2SnH_4 is less than zero. This means that the structure is thermodynamically stable and can be synthesized in the experimental setting.

In addition, the thermodynamic analysis of hydrogen desorption has revealed the most critical effect of alkali metal substitution. Parameters calculated using equations (2)–(4) show that hydrogen bonds in the Na_2SnH_4 structure are significantly weakened.

$$\Delta E_{reac} = E_{X_2Sn} + 2E_{H_2} - E_{X_2SnH_4} \quad (2)$$

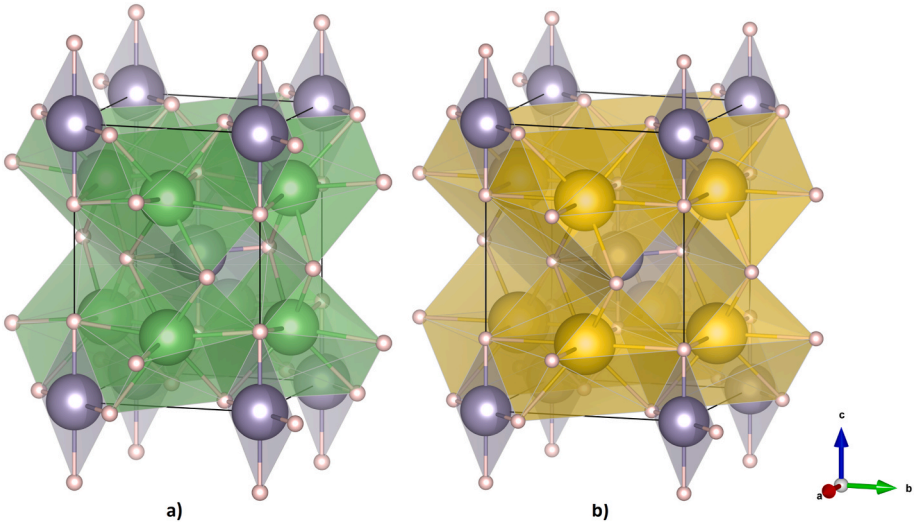

Fig. 1. Crystal structures of (a) Li_2SnH_4, and (b) Na_2SnH_4 compounds.

Table 2
Structural parameters of Li_2SnH_4 and Na_2SnH_4 compounds, including lattice constants (*a, b, c*) in Å, unit cell volume (Å^3), formation energy E_f (KeV/atom), gravimetric hydrogen storage capacity $G_{wt.}$, reaction energy (eV), Desorption Energy (eV/mol H_2), and Desorption Enthalpy (kJ/mol H_2).

Material	Lattice Constans	Volume	ΔE_f	$G_{wt.}$ (%)	References
Li_2SnH_4	4.344 4.344 6.255	118.035	−0.002	5.95	This Study
Na_2SnH_4	5.159 5.159 7.195	191.508	−0.049	4.82	This Study
		Reaction Energy	**Desorption Energy**	**Desorption Enthalpy**	**References**
Li_2SnH_4		0.91	0.46	44.11	This Study
Na_2SnH_4		0.82	0.41	39.44	This Study

$$\Delta E_{des}(per\ mol\ H_2) = \frac{\Delta E_{reac}}{2} \quad (3)$$

$$|\Delta H| = \frac{\Delta E_{reac}}{2} \times 96.485 \quad (4)$$

The total reaction energy (ΔEreac) decreased from 0.91 eV to 0.82 eV, while the desorption energy per mol H_2 decreased from 0.46 eV/mol H_2 to 0.41 eV/mol H_2. This is reflected in the desorption enthalpy (ΔH), the final and most important physical parameter: the value of 44.11 kJ/mol H_2 for Li_2SnH_4 has decreased to 39.44 kJ/mol H_2 for Na_2SnH_4, providing an improvement of approximately 10.6 %. The practical significance of the obtained ΔH values should be evaluated considering the 20–40 kJ/mol H_2 range, which is considered ideal for hydrogen storage materials. The calculated value of 39.44 kJ/mol H_2 for Na_2SnH_4 is extremely close to the upper limit of this range. This suggests that the material could theoretically exhibit reversible hydrogen release at temperatures around 80–120 °C, which are practically applicable temperatures. This value also shows a remarkable similarity to the desorption enthalpy (≈37 kJ/mol H_2) of sodium aluminate ($NaAlH_4$), a well-characterized reference material.

3.2. Electronic properties

To understand the hydrogen storage capacity of materials, not only structural and thermodynamic parameters but also their electronic properties must be investigated in detail. By examining the electronic band structure and density of states (DOS/PDOS), valuable information can be obtained regarding the conductivity character, band gap, and possible charge transfer mechanisms that occur during hydrogen adsorption. Particularly in hydrogen storage materials, the binding energies of hydrogen atoms with the host lattice or surface are directly related to the electronic structure. Therefore, electronic band structure calculations performed by density functional theory (DFT) not only determine whether the material exhibits metallic, semiconducting, or insulating behavior but also shed light on its hydrogen storage capacity. During the hydrogen storage process, the interaction between hydrogen molecules/atoms and the host material is directly influenced by the redistribution of electron density and transitions between the valence and conduction bands. If a material exhibits purely metallic behavior, the interaction with hydrogen is usually weak, making stable hydrogen storage difficult. On the other hand, insulating materials with a wide band gap restrict electron transfer, which limits hydrogen adsorption. In this regard, semiconducting materials with a moderate band gap are considered more suitable for hydrogen storage, since they allow sufficient charge transfer and provide a balanced adsorption/desorption mechanism.

As shown in Fig. 2, the band structure in panel (a) reveals a band gap of 0.678 eV. This relatively narrow band gap indicates that the material possesses a weak semiconducting character. The small energy difference between the valence band maximum (VBM) and conduction band minimum (CBM) allows electrons to be easily excited into the conduction band. This enhances the electrical conductivity of the material and plays a significant role in the adsorption and desorption of hydrogen atoms. In contrast, panel (b) exhibits a band gap of 1.251 eV, which is wider compared to panel (a) and corresponds to typical semiconducting behavior.

Such a band gap provides a favorable electronic environment for stable interaction with hydrogen. Therefore, this material may display a more stable and reliable hydrogen storage performance. Moreover, whether the band gap is direct or indirect can strongly affect the kinetic behavior of hydrogen within the material. The valence band represents the electrons that can participate in bonding during hydrogen adsorption, whereas the conduction band corresponds to the energy states where excited electrons may reside. Suppose the energy difference between the valence and conduction bands is narrow (as in Fig. 2-a). In that case, hydrogen adsorption/desorption processes can occur more easily, though maintaining hydrogen at high temperatures may be difficult. On the other hand, a wider band gap (as in Fig. 2-b) ensures more stable storage, but additional energy may be required for hydrogen release. Therefore, the ideal structure for hydrogen storage applications is typically a semiconductor with a moderate band gap.

The results obtained from DFT calculations reveal that the first material (Fig. 2-a) exhibits a more conductive character due to its narrow band gap, while the second one (Fig. 2-b) demonstrates typical semiconducting behavior. The absence of metallic characteristics is advantageous for hydrogen storage, since in metallic systems, hydrogen is usually weakly bound on the surface, leading to poor storage capacity. Overall, the analysis of electronic band structures highlights the

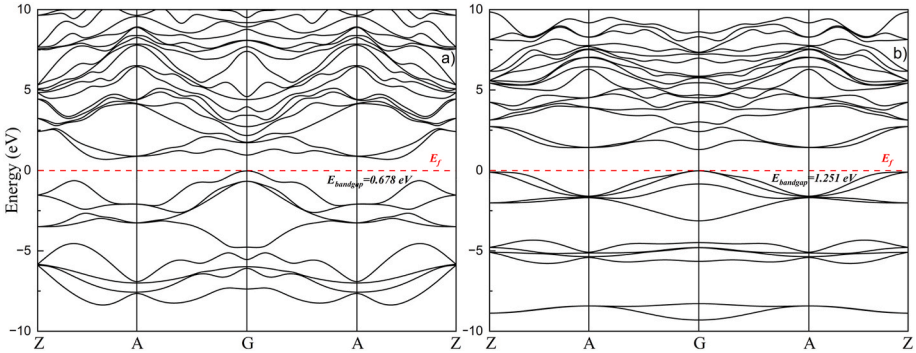

Fig. 2. Electronic band structure of (a) Li_2SnH_4, and (b) Na_2SnH_4 compounds calculated using the GGA-PBE functional.

fundamental electronic mechanisms that support the hydrogen storage performance of the investigated materials and provides critical insights into their potential applications. In addition to the band structure calculations, the total and partial density of states (DOS and pDOS) analyses provide further insights into the contribution of individual atomic orbitals to the electronic structure of the investigated systems. The DOS profiles are essential to understanding the hybridization between different orbitals, the localization of electronic states, and the mechanisms of charge transfer during hydrogen adsorption and desorption.

As shown in Fig. 3a, the total DOS and pDOS reveal that the Li-p and Sn-p orbitals mainly dominate the states around the Fermi level (Ef), while the H-s orbitals make significant contributions in the valence band region (−10 eV to −2 eV). The hybridization between the Sn-p and H-s orbitals indicates strong orbital overlap, which enhances the bonding interactions between Sn and H atoms. Furthermore, the relatively narrow band gap of 0.678 eV, already observed in the band structure, is also evident in the DOS spectrum, confirming the semiconducting nature of the material. The presence of Li-p orbitals in the conduction band suggests that Li plays a key role in charge transfer processes, facilitating electronic transitions that are crucial for hydrogen adsorption and release. In Fig. 3b, the DOS profile of the Na–Sn–H system exhibits a wider band gap of 1.251 eV, in agreement with the band structure calculations. The Na-p and Sn-p states dominate the conduction band region, while the H-s and Sn-s/p orbitals contribute significantly to the lower part of the valence band (below −5 eV). The strong contribution of H-s orbitals at deeper energy levels indicates stable bonding of hydrogen within the lattice. Compared to the Li-containing system, the Na-based compound shows reduced orbital overlap near the Fermi level, which explains the larger band gap and more pronounced semiconducting behavior. This suggests a more stable electronic environment for hydrogen storage, though hydrogen desorption may require slightly higher energy due to stronger localization of states.

The DOS analyses support the band structure results by confirming that both systems exhibit semiconducting behavior rather than metallic or insulating characteristics. The Li–Sn–H system, with its narrower band gap and higher density of electronic states near the Fermi level, may facilitate faster hydrogen adsorption and desorption dynamics. However, this could also reduce stability at elevated temperatures. Conversely, the Na–Sn–H system, with its wider band gap and stronger localization of hydrogen-related states, is expected to ensure more stable hydrogen retention, albeit with slightly higher energy requirements for release. These complementary electronic features demonstrate how subtle differences in electronic structure can strongly affect the hydrogen storage performance of materials.

3.3. Mechanical properties

The investigation of elastic properties is fundamental for understanding the mechanical performance, bonding characteristics, and potential technological applications of hydrides. In this study, the elastic constants of Li_2SnH_4 and Na_2SnH_4, both crystallizing in the tetragonal $P4_2/mnm$ space group, were calculated by means of density functional theory (DFT) within the GGA-PBE approximation. The obtained six independent elastic constants for tetragonal crystals (C_{11}, C_{12}, C_{13}, C_{33}, C_{44}, and C_{66}) are listed in Table 3 [34].

For a tetragonal crystal system, the Born stability criteria must be satisfied to ensure mechanical stability. The conditions are expressed as follows [34]:

$$C_{11} > 0, C_{33} > 0, C_{44} > 0, C_{66} > 0, (C_{11} - C_{12}) > 0$$

$$(C_{11} + C_{13} - 2C_{13}) > 0, (2C_{11} + C_{33} + 2C_{12} + 4C_{13}) > 0 \quad (5)$$

Satisfying these conditions ensures that the tetragonal lattice remains mechanically stable under applied stress and strain. Our results show that both Li_2SnH_4 and Na_2SnH_4 fulfill these requirements, confirming their mechanical stability in the tetragonal phase. The bulk modulus (B), shear modulus (G), and Young's modulus (E) were derived using the Voigt–Reuss–Hill (VRH) averaging scheme. Additional parameters, including Pugh's ratio (B/G), Zener anisotropy factor (A), and Poisson's ratio (ν), were also determined. The results are summarized in Table 4.

The bulk modulus (B) reflects the resistance of a material against volumetric compression. The higher bulk modulus of Li_2SnH_4 compared to Na_2SnH_4 indicates that Li_2SnH_4 is less compressible and thus mechanically stiffer. The shear modulus (G) measures resistance to shear deformation, while the Young's modulus (E) represents the overall stiffness under uniaxial stress. The calculated values clearly show that Li_2SnH_4 is mechanically stronger and more rigid than Na_2SnH_4. Poisson's ratio (ν) provides insights into the nature of atomic bonding. Typical covalent materials exhibit $\nu \approx 0.1$, ionic crystals $\nu \approx 0.25$, and metallic systems $\nu = 0.3$–0.5. The obtained values of 0.284 (Li_2SnH_4) and 0.277 (Na_2SnH_4) are close to 0.25, indicating predominantly ionic bonding characteristics in both compounds. The Pugh's ratio (B/G) is a reliable indicator of ductility versus brittleness. A critical value of 1.75 separates ductile (>1.75) from brittle (<1.75) behavior. Since both compounds exhibit B/G > 1.9, Li_2SnH_4 and Na_2SnH_4 are predicted to be ductile, which implies that they can withstand plastic deformation before fracture. The Zener anisotropy factor (A) evaluates the elastic anisotropy of tetragonal crystals, where a value of unity corresponds to isotropy. The obtained values (0.737 for Li_2SnH_4 and 1.191 for Na_2SnH_4) clearly deviate from 1, confirming anisotropic elastic behavior. Such anisotropy suggests that these compounds respond differently to stress depending on crystallographic direction, which is significant for practical applications where directional mechanical properties play a role.

The analysis reveals that the elastic properties of Li_2SnH_4 and Na_2SnH_4 directly influence their hydrogen storage performance. Li_2SnH_4, with higher stiffness, is expected to provide superior structural stability, making it resistant to degradation during repeated hydrogenation cycles. On the other hand, Na_2SnH_4, with lower bulk modulus

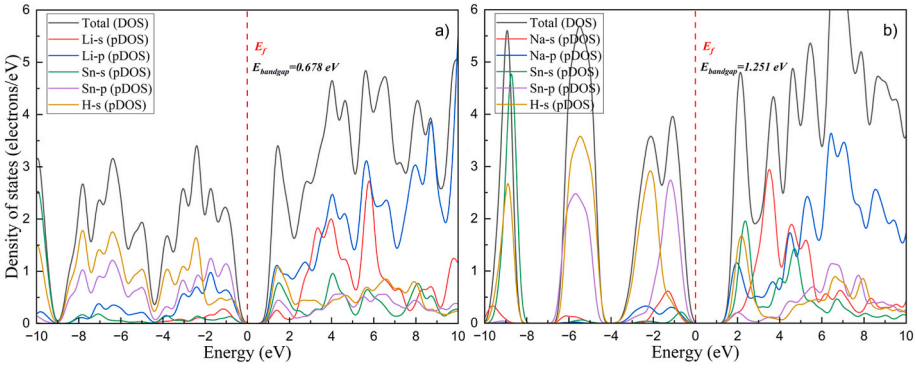

Fig. 3. Total and partial density of states (DOS)of (a) Li_2SnH_4, and (b) Na_2SnH_4 compounds calculated using the GGA-PBE functional.

Table 3
Elastic constants (C_{ij}) of Li_2SnH_4 and Na_2SnH_4 compounds (in GPa).

Material	C_{11}	C_{12}	C_{13}	C_{33}	C_{44}	C_{66}	References
Li_2SnH_4	112.262	5.700	51.035	100.938	39.266	15.097	This Study
Na_2SnH_4	67.472	40.530	16.928	65.278	16.050	32.498	This Study

Table 4
Derived mechanical properties of Li_2SnH_4 and Na_2SnH_4 compounds (in GPa), including bulk modulus (B), shear modulus (G), Young's modulus (E), Pugh's ratio (B/G), anisotropy factor (A), Poisson's ratio (ν), and Vicker Hardness H_V.

Material	B	G	E	B/G	A	υ	H_V	References
Li_2SnH_4	59.000	29.791	76.499	1.980	0.737	0.284	4.678	This Study
Na_2SnH_4	38.344	20.069	51.264	1.911	1.191	0.277	3.684	This Study

and higher anisotropy, may offer better volumetric adaptability and potentially enhanced hydrogen diffusion. Consequently, the balance between elastic rigidity and flexibility is crucial: while rigidity ensures structural durability, moderate flexibility promotes hydrogen uptake and release. This balance highlights that both compounds are promising hydrogen storage materials, but their performance may differ depending on whether durability (Li_2SnH_4) or diffusion kinetics (Na_2SnH_4) is prioritized.

3.4. Optical properties

Although the primary aim of this study is to evaluate the hydrogen storage potential of Li_2SnH_4 and Na_2SnH_4, the optical properties are presented to provide a comprehensive understanding of their electronic response. Examination of the dielectric function, absorption, reflectivity, and optical conductivity offers fundamental insight into the electronic transitions governing their band structures. Moreover, optical behavior can be relevant for assessing possible photochemical or photothermal activation pathways for hydrogen release, as reported in certain complex hydrides. Therefore, optical analysis serves both as a fundamental characterization and as a complementary perspective for evaluating potential light-assisted hydrogen release mechanisms.

The dielectric function is a function consisting of the sum of the real (ε_1) and imaginary (ε_2) parts, where the real (ε_1) part evaluates the compound's electrical energy storage capacity, and the imaginary part (ε_2) provides information about energy losses and absorption behavior. When examining Fig. 4, the maximum value of the real (ε_1) part indicates the maximum value of the compound's response to electron excitation.

The dielectric functions of Li_2SnH_4 and Na_2SnH_4 exhibit pronounced spectral features in both the real (ε_1) and imaginary (ε_2) components, reflecting their electronic structures and optical responses. For Li_2SnH_4, ε_1 begins with a relatively high static dielectric constant of about 12 and reaches a maximum above 15 near 2 eV, after which it rapidly decreases and becomes negative between 4 and 6 eV, indicating the presence of plasma resonance. At higher energies, ε_1 gradually approaches zero with small oscillations. The corresponding ε_2 spectrum shows the onset of optical absorption around 1.5–2 eV, followed by a strong peak at approximately 3–4 eV and additional pronounced features extending up to 10 eV, suggesting intense interband transitions within this range. In contrast, Na_2SnH_4 exhibits a lower static dielectric constant of about 6, with ε_1 reaching a peak close to 9 around 3 eV, crossing zero at 5 eV, and subsequently taking negative values between 8 and 15 eV, highlighting a lower-energy plasma frequency compared to Li_2SnH_4. The ε_2 function reveals an absorption onset at about 2 eV, a main peak around 4 eV, and a secondary strong feature between 6 and 8 eV before gradually decaying at higher energies. These findings indicate that Li_2SnH_4 possesses stronger polarizability and broader absorption characteristics, whereas Na_2SnH_4 exhibits more distinct absorption peaks at relatively lower energies, underscoring the influence of cation substitution on the optical response of Sn–H-based hydrides.

As shown in Fig. 5, the optical conductivity spectra of Li_2SnH_4 (a) and Na_2SnH_4 (b) exhibit characteristic differences in both the real (ε_1) and imaginary (ε_2) components, reflecting their distinct electronic responses. For Li_2SnH_4, the real part of conductivity displays a sharp increase starting around 2 eV, reaching a maximum above 6 (1/fs) near 5 eV, followed by a gradual decrease with secondary features extending up to 12 eV, and then slowly diminishing at higher energies. The imaginary part initially assumes negative values at low energies, showing a pronounced minimum near 2 eV, before crossing into positive values around 5 eV, exhibiting broad oscillations, and gradually stabilizing beyond 12 eV. In contrast, Na_2SnH_4 demonstrates a lower conductivity magnitude, with the real part peaking at approximately 4 (1/fs) around 4.5 eV and developing a secondary shoulder near 7–8 eV before decreasing at higher frequencies. The imaginary part also begins with negative values, reaching a minimum around 3 eV, then displaying alternating positive and negative oscillations up to ~8 eV, after which it becomes predominantly positive and decreases slowly at higher energies. These findings suggest that Li_2SnH_4 possesses stronger optical conductivity with broader spectral features, whereas Na_2SnH_4 exhibits

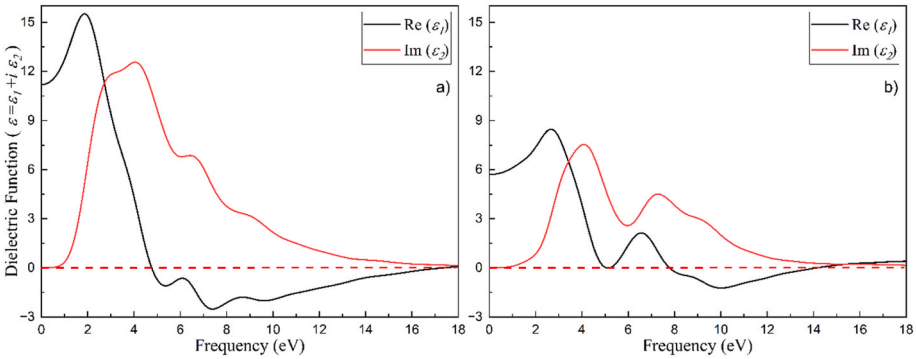

Fig. 4. The optical dielectric function for the $P4_2/mnm$ phases of (a) Li_2SnH_4 and (b) Na_2SnH_4. The calculations are for the polycrystalline form.

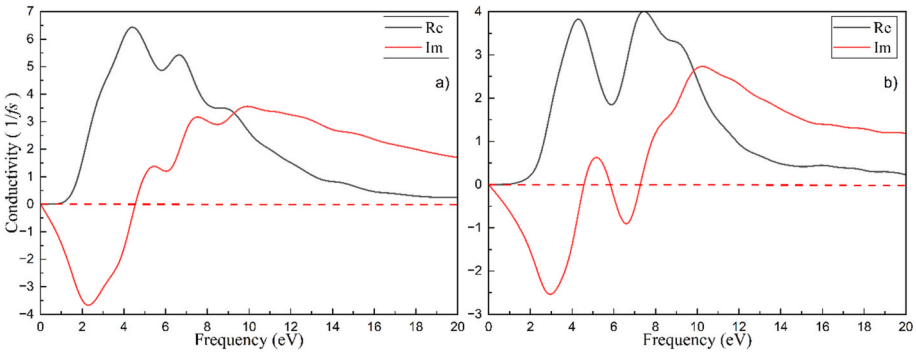

Fig. 5. The optical conductivity (1/fs) for the $P4_2/mnm$ phases of (a) Li_2SnH_4 and (b) Na_2SnH_4. The calculations are for the polycrystalline form.

relatively weaker but more structured conductivity peaks, underscoring the role of cation substitution in modulating charge-carrier dynamics and interband transition strength.

As shown in Fig. 6, the reflectivity spectra of Li_2SnH_4 and Na_2SnH_4 exhibit distinct optical responses that highlight the influence of cation substitution. Li_2SnH_4 starts with a relatively high initial reflectivity of about 28 % at low photon energies and displays multiple pronounced peaks in the 4.5–16 eV range, reaching a maximum of nearly 55 %. This behavior indicates strong optical reflection over a broad energy window, suggesting the presence of plasmonic resonances. At higher energy levels, the reflectivity gradually decreases and drops sharply above 22 eV, approaching nearly zero. In contrast, Na_2SnH_4 begins with a lower initial reflectivity of ~17 % and shows sharper variations with characteristic peaks and valleys between 4 and 12 eV, reaching a maximum of about 42 %. However, compared to Li_2SnH_4, the spectrum is narrower, and the reflectivity declines more rapidly above 15 eV, becoming very small after ~20 eV. These results demonstrate that Li_2SnH_4 exhibits stronger and broader optical reflectivity, while Na_2SnH_4 provides more confined reflectivity features at lower photon energies.

The absorption spectra of Li_2SnH_4 and Na_2SnH_4, as illustrated in Fig. 7, exhibit distinct features that reflect their electronic transition dynamics. For Li_2SnH_4 (black curve), absorption begins sharply at low photon energies and reaches a pronounced maximum of over 2.5×10^5 cm^{-1} around 7–9 eV, followed by multiple secondary peaks that gradually decrease in intensity up to ~20 eV. Beyond this region, the spectrum shows weaker oscillatory features that eventually diminish at higher energy levels. In contrast, Na_2SnH_4 (red curve) displays a relatively lower overall absorption magnitude, with the main absorption peak appearing near 8–10 eV at ~2.1×10^5 cm^{-1}, accompanied by a noticeable shoulder around 5 eV. Its absorption intensity decreases more rapidly compared to Li_2SnH_4, although residual structures persist up to ~40 eV, indicating more localized transitions at higher energies. These results highlight that Li_2SnH_4 possesses stronger and broader absorption in the ultraviolet range, while Na_2SnH_4 exhibits comparatively weaker but more structured spectral features.

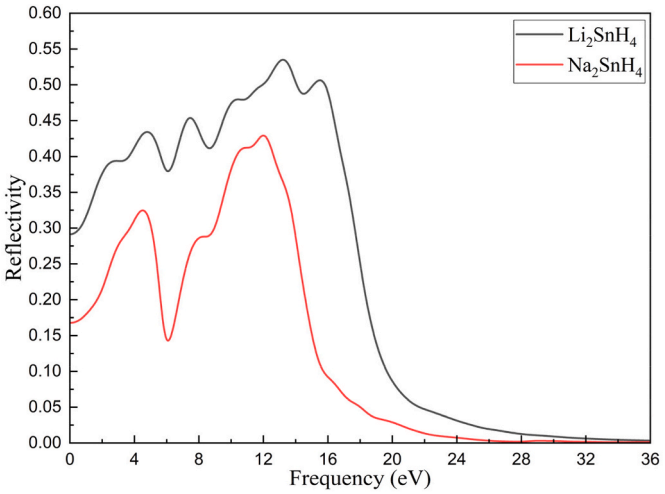

Fig. 6. The optical reflectivity for the $P4_2/mnm$ phases of (a) Li_2SnH_4 and (b) Na_2SnH_4. The calculations are for the polycrystalline form.

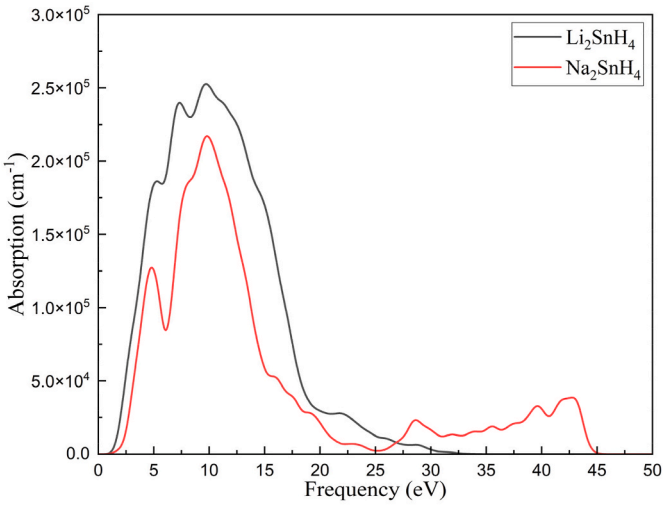

Fig. 7. The optical absorption (cm^{-1}) for the $P4_2/mnm$ phases of (a) Li_2SnH_4 and (b) Na_2SnH_4. The calculations are for the polycrystalline form.

The optical properties of Li_2SnH_4 and Na_2SnH_4 exhibit clear differences in their electronic responses. Li_2SnH_4 shows higher conductivity, stronger reflectivity, and broader absorption features, indicating enhanced optical activity across a wide spectral range. In contrast, Na_2SnH_4 displays weaker but more structured peaks, with comparatively lower intensity in conductivity, reflectivity, and absorption. These results highlight the crucial role of cation substitution in modulating the optical behavior of Sn-based hydrides [34].

3.5. Vibrational properties

The investigation of phonon band structures is of great importance for evaluating the dynamic stability as well as understanding the hydrogen storage performance of materials. The presence of only positive phonon frequencies indicates that the structure is dynamically stable, confirming its potential applicability in hydrogen storage systems. In this context, the phonon dispersions of Li_2SnH_4 and Na_2SnH_4 compounds along the high-symmetry points were calculated and are presented in Fig. 8. For Li_2SnH_4, the absence of imaginary frequencies in the phonon spectrum demonstrates that the structure is dynamically stable. The acoustic branches located in the low-frequency region (0–6 THz) mainly originate from the collective vibrations of Li and Sn atoms.

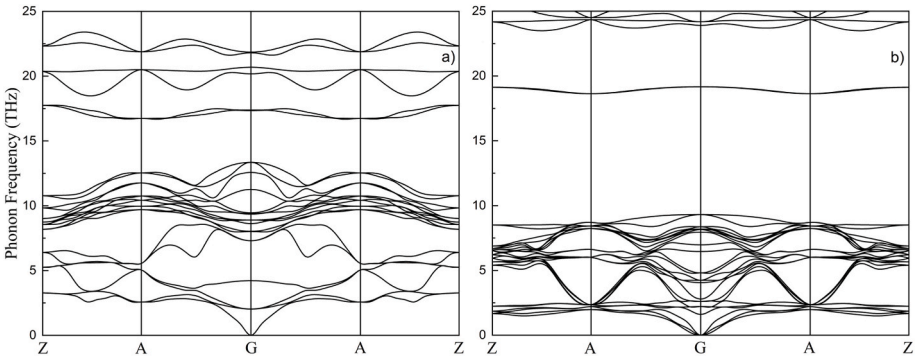

Fig. 8. Phonon dispersion curves of (a) Li_2SnH_4 and (b) Na_2SnH_4 compounds along the high-symmetry directions of the Brillouin zone.

The high-frequency modes are concentrated within the range of 10–25 THz, which are essentially attributed to the vibrations of the light hydrogen atoms. A clear separation between acoustic and optical branches indicates the presence of strong bonding interactions in the system. In particular, the contribution of hydrogen atoms to high-frequency modes suggests that hydrogen atoms in Li_2SnH_4 are strongly bonded, which may lead to high hydrogen storage capacity. However, the broad distribution of the optical branches also implies that hydrogen is tightly bound in the structure, indicating that hydrogen desorption may require relatively higher temperatures.

In the case of Na_2SnH_4, the phonon spectrum also reveals no negative frequencies, confirming its dynamical stability. However, compared to Li_2SnH_4, the high-frequency modes are shifted to lower energy ranges. The optical modes are mainly concentrated between 8 and 20 THz, suggesting weaker bonding interactions of hydrogen atoms than in Li_2SnH_4. Moreover, the narrower frequency range of the acoustic modes reflects a more flexible vibrational behavior, implying that hydrogen atoms can move more easily within the lattice. This characteristic suggests that Na_2SnH_4 may exhibit lower energy barriers during hydrogen release and therefore possess a kinetic advantage. In both compounds, the unit cell contains a total of 7 atoms (2 Li/Na +1 Sn + 4H), which gives rise to 21 phonon branches in total, including 3 acoustic and 18 optical modes. While the acoustic modes are located at lower frequencies, the optical branches—dominated by the contribution of hydrogen atoms—are observed in the high-frequency region. The relatively large number of optical modes and their high-frequency positions clearly demonstrate the dominant vibrational role of hydrogen atoms in these compounds.

To obtain deeper insight into the thermodynamic stability of X_2SnH_4 (X = Li, Na), we correlated the phonon dispersion curves with the projected density of states (PDOS). The low-frequency acoustic modes are mainly associated with the heavier Sn and X (Li/Na) atoms, whereas the high-frequency optical modes originate predominantly from H vibrations, in agreement with the atom-resolved PDOS. The absence of imaginary frequencies throughout the Brillouin zone, together with this consistent mapping between the phonon branches and PDOS, confirms the dynamical stability of both hydrides and provides a coherent picture of their vibrational and thermodynamic behavior.

In conclusion, Li_2SnH_4 exhibits higher-frequency modes, indicating stronger hydrogen bonding, while Na_2SnH_4 shows lower-frequency optical modes, implying weaker bonding of hydrogen atoms. This suggests that Li_2SnH_4 may provide higher storage capacity, whereas Na_2SnH_4 could offer more favorable release conditions. Therefore, the investigation of phonon properties not only verifies the dynamic stability of these materials but also provides fundamental insights into their hydrogen storage performance.

3.6. Thermal properties

The thermal properties of Li_2SnH_4 and Na_2SnH_4 compounds were evaluated by analyzing the behavior of heat capacity (cal/cell*K) and Debye temperature (Θ_D) [35,36]. The temperature-dependent heat capacities of Li_2SnH_4 and Na_2SnH_4 are presented in Fig. 9.

Both compounds exhibit a rapid increase in heat capacity (cal/cell*K) at low temperatures, followed by a gradual approach toward saturation in accordance with the Dulong–Petit limit [37–39]. Na_2SnH_4 shows a faster increase in the low-temperature regime compared to Li_2SnH_4, which can be attributed to stronger phonon contributions arising from the heavier Na atom. Throughout the entire temperature range, the heat capacity (cal/cell*K) of Na_2SnH_4 remains higher than that of Li_2SnH_4, indicating that Na substitution enhances the vibrational degrees of freedom of the system. Furthermore, the onset of the plateau region occurs at approximately 500 K for Na_2SnH_4 and 600 K for Li_2SnH_4. These results emphasize the significant influence of alkali metal size on the thermodynamic behavior of Sn-based hydrides.

Fig. 10 illustrates the variation of Debye temperature (Θ_D) as a function of temperature for Li_2SnH_4 and Na_2SnH_4 compounds. In both systems, Θ_D increases monotonically with temperature, reflecting the enhanced lattice vibrations and phonon activity at elevated temperatures. At low temperatures, both compounds display relatively low Debye temperatures (~200 K), but Li_2SnH_4 consistently exhibits higher Θ_D values compared to Na_2SnH_4 across the entire investigated range. For instance, at 1000 K, the Debye temperature of Li_2SnH_4 reaches approximately 2300 K, whereas Na_2SnH_4 attains about 1600 K.

The systematically higher Θ_D observed in Li_2SnH_4 can be attributed to the smaller atomic mass of Li compared to Na, which leads to stronger

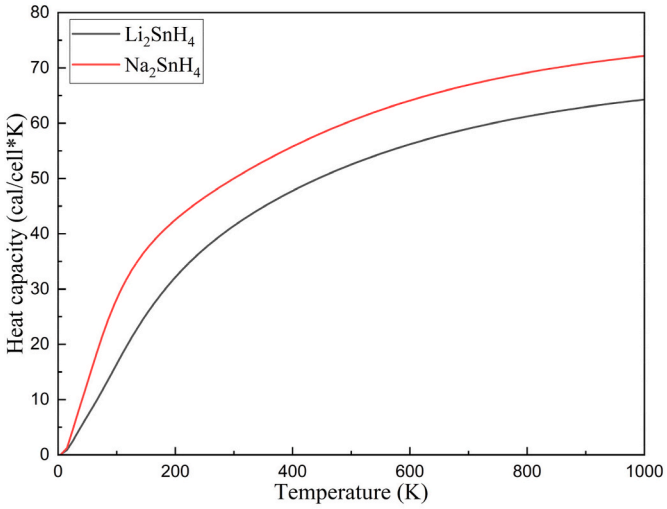

Fig. 9. The heat capacity curve for the $P4_2/mnm$ phases of Li_2SnH_4 (black curve) and Na_2SnH_4 (red curve) compounds. (For interpretation of the references to colour in this figure legend, the reader is referred to the Web version of this article.)

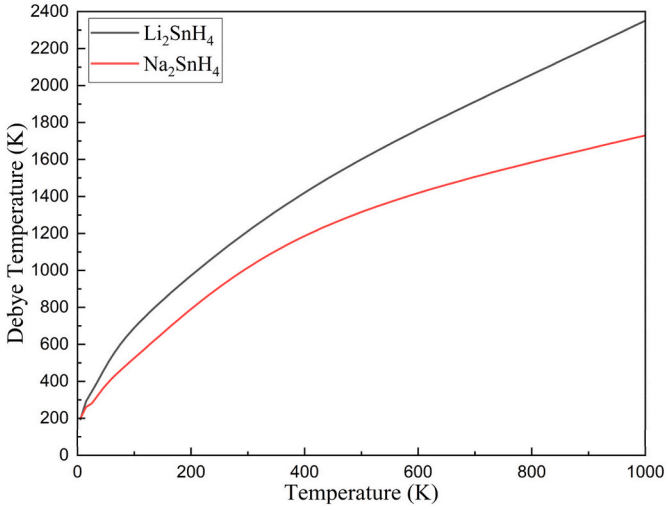

Fig. 10. The Debye temperature curve for the $P4_2/mnm$ phases of Li_2SnH_4 (black curve) and Na_2SnH_4 (red curve) compounds. (For interpretation of the references to colour in this figure legend, the reader is referred to the Web version of this article.)

interatomic bonding and higher lattice stiffness. This behavior indicates that Li_2SnH_4 possesses superior phonon frequencies and, consequently, greater thermal stability and rigidity. Conversely, the lower Θ_D of Na_2SnH_4 suggests weaker bonding strength and softer lattice dynamics. These findings emphasize the crucial role of alkali metal substitution in tailoring the vibrational and thermodynamic properties of Sn-based hydrides, with Li incorporation leading to stiffer and more thermally stable structures.

3.7. Hydrogen storage properties

The hydrogen storage performance of Li_2SnH_4 and Na_2SnH_4 were evaluated by combining their gravimetric capacities with thermal and vibrational properties. The calculated hydrogen storage capacities are 5.95 wt% for Li_2SnH_4 and 4.82 wt% for Na_2SnH_4, indicating that both compounds possess promising storage potential, with Li_2SnH_4 exhibiting a higher capacity due to the lighter atomic mass of lithium. A wide variety of complex and perovskite-type hydrides have been explored as hydrogen storage materials, yet most reported systems still exhibit limited gravimetric capacities. For instance, AFe_3H_8 hydrides (A = Na, K, Rb) [40] show capacities up to only 4.23 wt%, while Be-based perovskites such as $BePdH_3$, $BeAgH_3$, and $BeCdH_3$ exhibit even lower values of 2.49, 2.46, and 2.37 wt%, respectively [41]. Similarly, Mn_3NaH_8 and Mn_3KH_8 provide moderate values of 4.117 wt% and 3.804 wt% [42]. Additional hydride families—including X_2CaTiH_6 (X = Li, Na) [43], XFe_3H_8 (X = Mg, Na, Sr) [44], and LiX_3H_8 (X = Ni, Mn) [45]—also remain within a comparable capacity range, not surpassing the 4–5 wt% threshold. Recently reported LiX_3H_8 (X = Fe, Cr) [46], as well as double perovskites X_2CaAlH_6 (X = K, Rb, Cs) [19], likewise offer gravimetric capacities below the U.S. DOE target of 5 wt%. Even the more promising X_2MgTiH_6 double perovskites (X = Li, Na, K) [47] reach capacities of 6.16 wt%, 4.64 wt%, and 3.72 wt%, respectively, indicating that only the Li-based composition slightly exceeds the 5 wt% mark. In comparison with all these systems, the gravimetric hydrogen storage capacities obtained in this work—5.95 wt% for Li_2SnH_4 and 4.82 wt% for Na_2SnH_4—demonstrate that Sn-based hydrides outperform most known perovskite and complex hydrides. This superior performance highlights X_2SnH_4 compounds as strong candidates for next-generation lightweight hydrogen storage materials.

The calculated heat capacities (cal/cell*K) increase rapidly at low temperatures and gradually approach the Dulong–Petit limit at elevated temperatures. Na_2SnH_4 shows a steeper rise in the low-temperature regime, suggesting stronger phonon contributions from the heavier sodium atom, whereas Li_2SnH_4 demonstrates a more stable thermal response. The Debye temperature further emphasizes these differences, with Li_2SnH_4 maintaining significantly higher Θ_D values across the entire temperature range (~2300 K at 1000 K) compared to Na_2SnH_4 (~1600 K at 1000 K). The higher Θ_D of Li_2SnH_4 reflects stronger interatomic bonding and greater lattice stiffness, which enhances its thermal stability during hydrogen storage and release cycles. In contrast, the relatively lower Θ_D of Na_2SnH_4 indicates softer lattice dynamics, which may facilitate hydrogen diffusion and potentially improve release kinetics. When compared directly, Li_2SnH_4 demonstrates superior storage density and structural stability, whereas Na_2SnH_4 may offer advantages in terms of phonon-mediated hydrogen mobility. Compared to other complex hydrides, such as $NaAlH_4$ (~5.6 wt%) [48,49] and $LiBH_4$ (~18.5 wt%, though with high desorption temperatures) [50–52], both Li_2SnH_4 and Na_2SnH_4 exhibit a favorable balance between hydrogen capacity and thermodynamic stability. These findings suggest that Sn-based hydrides, particularly Li_2SnH_4, are promising candidates for solid-state hydrogen storage, with the potential for further optimization through doping strategies or catalytic modification to improve kinetics and cycling performance. A meaningful evaluation of hydrogen release behavior requires comparing the desorption temperatures of the present X_2SnH_4 hydrides with those reported for other complex hydrides in the literature. For the $BaXH_3$ (X = Tc, Ta, Mo) [21] perovskite hydrides, reported desorption temperatures fall in the range of 317–501 K, as shown in the referenced thermal analyses. Similarly, the $RbXH_3$ (X = Cr, Zr) [53] systems exhibit desorption temperatures within a comparable interval, also between 317 K and 501 K, reflecting the strong metal–hydrogen bonding in these heavier perovskites. In contrast, the LiX_3H_8 (X = Fe and Cr) [46] hydrides show significantly lower desorption temperatures of 332.936 K ($LiFe_3H_8$) and 322.601 K ($LiCr_3H_8$), indicating more moderate hydrogen release behavior and enhanced practical usability under mild conditions. When compared with these systems, the desorption temperatures predicted in the present study for Li_2SnH_4 and Na_2SnH_4 demonstrate that Sn-based hydrides possess thermodynamic characteristics competitive with or superior to many known perovskite and complex hydrides, further supporting their potential as promising candidates for efficient hydrogen storage applications.

This work represents the first comprehensive study to calculate and report the structural, mechanical, vibrational, electronic, thermal, and hydrogen storage properties of Li_2SnH_4 and Na_2SnH_4, thereby providing novel insights into their potential for solid-state hydrogen storage applications.

4. Conclusions

We have performed a comprehensive first-principles investigation of Li_2SnH_4 and Na_2SnH_4 (tetragonal $P4_2/mnm$) covering structural, electronic, mechanical, vibrational, thermal, optical, and hydrogen-storage properties. Both compounds are found to be mechanically and dynamically stable in the optimized tetragonal phase, and they exhibit complementary characteristics that make them promising candidates for solid-state hydrogen storage. Structurally and electronically, both systems are semiconductors with moderate band gaps (0.678 eV for Li_2SnH_4 and 1.251 eV for Na_2SnH_4). From a mechanical standpoint, the calculated second-order elastic constants satisfy the Born stability conditions for tetragonal crystals, confirming elastic stability. The polycrystalline moduli obtained via the Voigt–Reuss–Hill averaging show that Li_2SnH_4 is mechanically stiffer than Na_2SnH_4 (B ≈ 59.0 GPa, G ≈ 29.8 GPa, E ≈ 76.5 GPa for Li_2SnH_4; B ≈ 38.3 GPa, G ≈ 20.1 GPa, E ≈ 51.3 GPa for Na_2SnH_4). Both compounds display B/G ratios >1.75 (indicating ductile behavior), Poisson's ratios around 0.28 (consistent with significant ionic character), and Zener anisotropy factors that deviate from unity (indicating elastic anisotropy). Vibrational and thermal analyses further distinguish between the two hydrides. Phonon

calculations reveal no imaginary modes for either compound, confirming dynamical stability. Li_2SnH_4 exhibits higher-frequency optical phonons (consistent with stronger H–Sn bonding) and higher Debye temperatures (indicative of a stiffer lattice and greater thermal stability), while Na_2SnH_4 shows lower-frequency optical modes and a softer lattice—characteristics that can facilitate hydrogen release and diffusion.

In terms of hydrogen storage performance, the calculated gravimetric capacities are substantial: 5.95 wt% for Li_2SnH_4 and 4.82 wt% for Na_2SnH_4. The higher capacity of Li_2SnH_4 reflects the lighter mass of Li and the stronger bonding framework that permits more hydrogen per unit mass, whereas Na_2SnH_4's softer lattice and weaker H–Sn bonding point to potentially easier desorption and faster kinetics. Thus, Li_2SnH_4 appears advantageous when capacity and cycle durability are prioritized, while Na_2SnH_4 may be preferred where lower desorption barriers and faster kinetics are required.

CRediT authorship contribution statement

Cengiz Soykan: Writing – review & editing, Writing – original draft, Methodology, Investigation. **Cihan Kürkçü:** Writing – review & editing, Writing – original draft, Methodology, Investigation, Funding acquisition.

Declaration of generative AI and AI-assisted technologies in the writing process

During the preparation of this work, the author(s) used an artificial intelligence tool to improve the language and readability of the study. After using this tool/service, the author(s) reviewed and edited the content as needed and took(s) full responsibility for the content of the publication.

Declaration of competing interest

The authors declare that they have no known competing financial interests or personal relationships that could have appeared to influence the work reported in this paper.

Acknowledgment

This study was supported by the Kırşehir Ahi Evran University under Scientific Research Project No: TBY.A1.24.001.

References

[1] Schlapbach L, Züttel A. Hydrogen-storage materials for mobile applications. Nature 2001;414:353–8. https://doi.org/10.1038/35104634.
[2] Ermiş S, İyigör A, Kürkçü C. Investigation of K2TiH6 and Ca2TiH6 under pressures from 0 to 20 GPa: structural, electronic, thermodynamic, mechanical, vibrational, and hydrogen storage properties. Int J Hydrogen Energy 2025;177:151653.
[3] Yamçıçıer Ç, Kürkçü C. Structural, elastic, optic, electronic, phonon, thermodynamic, and hydrogen storage properties of bialkali alanates M2LiAlH6 (M= Na, K). Int J Hydrogen Energy 2025;135:440–56.
[4] Züttel A. Hydrogen storage methods. Naturwissenschaften 2004;91:157–72. https://doi.org/10.1007/s00114-004-0516-x.
[5] Orimo SI, Nakamori Y, Eliseo JR, Züttel A, Jensen CM. Complex hydrides for hydrogen storage. Chemical reviews 2007;107(10):4111–32. https://doi.org/10.1021/cr0501846.
[6] Yamçıçıer Ç, Kürkçü C. Ab initio study of the structural, mechanical, optoelectronic and thermo-physical properties of XGaH5 (X= Ba, Ca, and Mg) compounds for hydrogen storage applications. Int J Hydrogen Energy 2024;81:391–404.
[7] Yamçıçıer Ç, Kürkçü C. Investigation of structural, electronic, elastic, vibrational, thermodynamic, and optical properties of Mg2NiH4 and Mg2RuH4 compounds used in hydrogen storage. J Energy Storage 2024;84:110883.
[8] Jain IP, Lal C, Jain A. Hydrogen storage in Mg: a most promising material. Int J Hydrogen Energy 2010;35:5133–44. https://doi.org/10.1016/j.ijhydene.2009.08.088.
[9] Gao G, Oganov AR, Li P, Li Z, Wang H, Cui T, et al. High-pressure crystal structures and superconductivity of stannane (SnH_4). Proc Natl Acad Sci USA 2010;107:1317–20. https://doi.org/10.1073/pnas.0908342107.
[10] Tahir M, Usman M, Rehman JU, Tahir MB. A first-principles study to investigate the physical properties of Sn-based hydride perovskites XSnH3 (X = K, Li) for hydrogen storage application. Int J Hydrogen Energy 2024;50:845–53. https://doi.org/10.1016/j.ijhydene.2023.08.145.
[11] Klopčič N, Grimmer I, Winkler F, Sartory M, Trattner A. A review on metal hydride materials for hydrogen storage. J Energy Storage 2023;72:108456. https://doi.org/10.1016/j.est.2023.108456.
[12] Almahmoud A, Alkhalidi H, Obeidat A. Comprehensive DFT analysis of structural, mechanical, electronic, optical, and hydrogen storage properties of novel perovskite-type hydrides Y_2CoH_6 (YCa, Ba, Mg, Sr). J Energy Storage 2025;117:116146.
[13] Al-Zoubi N, Almahmoud A, Almahmoud A, Obeidat A. Theoretical assessment of a novel NaXH3 and KXH3 (X= Tc, Ru and Rh) perovskite hydrides for hydrogen storage. Int J Hydrogen Energy 2024;93:822–31.
[14] Obeidat A, Almahmoud A, Alkhalidi H, Gharaibeh M. First-principles examination of the structural, hydrogen storage, mechanical, electronic, and optical properties of K2BAl1-xGaxH6 (BLi, Na; x= 0, 0.25, 0.5, 0.75, 1) double perovskite hydrides. Int J Hydrogen Energy 2025;153:150286.
[15] Obeidat A, Abu-Rajouh S, Almahmoud A, Aledealat K. Tunable hydrogen storage in double perovskite hydrides $K_2NaA1\text{-}xBxH_6$ (a, B= Al, Ga, and Sc): a first-principles study of structural, mechanical, electronic, and thermodynamic properties. Mater Sci Eng, B 2025;323:118889.
[16] Al-Qawasmeh A, Abu-Rajouh S, Al-Mahmoud A, Al-Khaldi H, Obeidat A. Ab initio analysis of the structural, hydrogen storage, mechanical, electronic, and optical characteristics of Cs2XAlH6 (X= K, Na, Rb) double perovskite hydrides. Sci Rep 2025;15:1–20.
[17] Obeidat A, Isied S, Alkhalidi H, Almahmoud A, Jaradat A. Structural, electronic, mechanical, dynamical, and optical properties of Kx3h8 (X= Sc, V, and Cr) hydrides: a dft perspective. Available at: SSRN 5208670 n.d.
[18] Almahmoud A, Alkhalidi H, Obeidat A. First-principles investigation of hydrogen storage in novel X₂Feh₅ hydrides (X= Ca, Mg, Ba). Available at: SSRN 5034496 2025.
[19] Alkhalidi H, Isied S, Almahmoud A, Obeidat A. Theoretical investigation of double perovskite hydrides X2CaAlH6 (X= K, Rb, and Cs) for hydrogen storage applications. Available at: SSRN 5134289 n.d.
[20] Eddahmani O, Hadhoud M, Tahiri A, Hassani AOT, Touti R. DFT-based study of NaYH3 and NaWH3 perovskite hydrides: structural, mechanical, electronic, and optical insights for hydrogen storage. Next Mater 2025;9:101150.
[21] Lemziouka A, Azdad A, Lemziouka H, Boutahar A, Tahiri A, Mrharrab L. First-principles calculations to investigate structural, elastic, phonon, electronic, and optical properties of BaXH3 (X= Tc, Ta, and Mo) perovskite-type hydrides for hydrogen storage applications. J Power Sources 2025;653:237710.
[22] Bahhar S, Tahiri A, Jabar A, Louzazni M, Idiri M, Bioud H. Computational assessment of MgXH3 (X= Al, Sc and Zr) hydrides materials for hydrogen storage applications. Int J Hydrogen Energy 2024;58:259–67.
[23] Benaali H, Bahhar S, Tahiri A, Didi Y, Fatihi H, Abbassi A, et al. Investigation of KMnH3 and KFeH3 perovskite hydrides via ab-initio for hydrogen storage. Inorg Chem Commun 2024;169:113033.
[24] Bahhar S, Jabar A, Tahiri A, Moubah R, Idiri M, Bioud H. X2CoH5 (X= Ca, Sr) for hydrogen storage: first-principles computations. Int J Hydrogen Energy 2024;83:1320–30.
[25] Clark SJ, Segall MD, Pickard CJ, Hasnip PJ, Probert MIJ, Refson K, et al. First principles methods using CASTEP. Z Kristallogr Cryst Mater 2005;220:567–70. https://doi.org/10.1524/zkri.220.5.567.65075.
[26] Kresse G, Furthmüller J. Efficiency of ab-initio total energy calculations for metals and semiconductors using a plane-wave basis set. Comput Mater Sci 1996;6:15–50.
[27] Kresse G, Furthmüller J. Efficient iterative schemes for *ab initio* total-energy calculations using a plane-wave basis set. Phys Rev B 1996;54:11169–86. https://doi.org/10.1103/PhysRevB.54.11169.
[28] Kresse G, Hafner J. Norm-conserving and ultrasoft pseudopotentials for first-row and transition elements. J Phys Condens Matter 1994;6:8245.
[29] Perdew JP, Burke K, Ernzerhof M. Generalized gradient approximation made simple. Phys Rev Lett 1996;77:3865–8. https://doi.org/10.1103/PhysRevLett.77.3865.
[30] Monkhorst HJ, Pack JD. Special points for Brillouin-zone integrations. Phys Rev B 1976;13:5188–92. https://doi.org/10.1103/PhysRevB.13.5188.
[31] Fischer TH, Almlof J. General methods for geometry and wave function optimization. J Phys Chem 1992;96:9768–74. https://doi.org/10.1021/j100203a036.
[32] Tkatchenko A, Scheffler M. Accurate Molecular Van Der Waals Interactions from Ground-State Electron Density and Free-Atom Reference Data. Phys Rev Lett 2009;102:073005. https://doi.org/10.1103/PhysRevLett.102.073005.
[33] Momma K, Izumi F. VESTA: a three-dimensional visualization system for electronic and structural analysis. Appl Crystallogr 2008;41:653–8.
[34] Soykan C, Kürkçü C. First-principles calculations to investigate structural, electronic, mechanical, optical, vibrational, thermal properties, and hydrogen storage capabilities of Rb2SnH4 for hydrogen storage applications. J Phys Chem Solid 2025;200:112618. https://doi.org/10.1016/j.jpcs.2025.112618.
[35] Baroni S. Phonons and related crystal properties from density-functional perturbation theory. Rev Mod Phys 2001;73:515–62. https://doi.org/10.1103/RevModPhys.73.515.
[36] Ashcroft NW, Mermin ND. In: Solid state. Physics, vol. 1. New York: Holt, Rinehart and Winston; 1976. Appendix C.
[37] Warren MC, Ackland GJ. Ab initio studies of structural instabilities in magnesium silicate perovskite. Phys Chem Miner 1996;23. https://doi.org/10.1007/BF00202306.

[38] Warren MC, Ackland GJ, Karki BB, Clark SJ. Phase transitions in silicate perovskites from first principles. Mineral Mag 1998;62:585–98.
[39] Anderson OL. A simplified method for calculating the Debye temperature from elastic constants. J Phys Chem Solid 1963;24:909–17.
[40] El Fatouaki Z, Tahiri A, Jabar A, Idiri M. Novel alkali metal AFe3H8 (A= Na, K, Rb) hydrides explored by first-principles calculations for hydrogen storage. Int J Hydrogen Energy 2025;183:151849.
[41] Benaali H, Didi Y, Tahiri A, Fatihi H, Touti R, Naji M. An ab-initio study of physical properties of BeXH3 (X= Pd, Ag, and Cd) perovskites hydrides for hydrogen storage applications. Int J Hydrogen Energy 2025;180:151745.
[42] El Fatouaki Z, Tahiri A, Jabar A, Idiri M. Designing Mn3NaH8 and Mn3KH8 hydride perovskites for efficient hydrogen storage via density functional theory. Int J Hydrogen Energy 2025;175:151433.
[43] Mekkaouy AE, Tahiri A, Chtita S, Touti R. First principles computational study of X2CaTiH6 (X= Li, and Na) for hydrogen storage applications. Int J Hydrogen Energy 2025;164:150723.
[44] Yildiz YG, Yıldız GD, İyigör A, Arikan N. A comprehensive DFT analysis of the structural, mechanical, electronic, and phonon properties of intermetallic XFe3H8 (X= Mg, Na, and Sr) hydrides. Mechanical, Electronic, and Phonon Properties of Intermetallic XFe3H8 (X= Mg, Na, and Sr) Hydrides n.d.
[45] El Fatouaki Z, Tahiri A, Jabar A, Idiri M. First-principles study on the physical properties of double perovskites LiX3H8 (X= Ni and Mn) for hydrogen storage. J Phys Chem Solid 2025:112867.
[46] El Fatouaki Z, Tahiri A, Jabar A, Idiri M. Comprehensive first-principles and AIMD study of alkali metal LiX3H8 (X= Fe, Cr) hydrides for hydrogen storage applications. Int J Hydrogen Energy 2025;163:150791.
[47] Touti R, El Mekkaouy A, Didi Y, Tahiri A, Chtita S. Computational analysis of X2MgTiH6 (X= Li, Na, and K) double perovskite hydride materials for hydrogen storage applications. Int J Hydrogen Energy 2025;161:150644.
[48] Jensen CM, Gross KJ. Development of catalytically enhanced sodium aluminum hydride as a hydrogen-storage material. Appl Phys A 2001;72:213–9. https://doi.org/10.1007/s003390100784.
[49] Fakioğlu E, Yürüm Y, Veziroğlu TN. A review of hydrogen storage systems based on boron and its compounds. Int J Hydrogen Energy 2004;29:1371–6.
[50] Soulié J-P, Renaudin G, Černý R, Yvon K. Lithium boro-hydride LiBH4: I. Crystal structure. J Alloys Compd 2002;346:200–5.
[51] Züttel A, Rentsch S, Fischer P, Wenger P, Sudan PH, Mauron P, et al. Hydrogen storage properties of LiBH4. J Alloys Compd 2003;356:515–20.
[52] Schlapbach L, Züttel A. Hydrogen-storage materials for mobile applications. Nature 2001;414:353–8.
[53] Al-Anazy M mana, Mustafa GM, Zayed O, Younas B, Al-Daraghmeh TM, Alkhaldi ND, et al. Study of alkaline metals hydrides RbXH3 (X = Mg/Ca/Sr/Ba) for green energy and hydrogen storage applications. Int J Hydrogen Energy 2024;78:927–37. https://doi.org/10.1016/j.ijhydene.2024.06.373.